Visualization and characterization of individual type III protein secretion machines in live bacteria

Article *in* Proceedings of the National Academy of Sciences · May 2017

DOI: 10.1073/pnas.1705823114

4 authors, including:

Yongdeng Zhang
Yale University
37 PUBLICATIONS **308** CITATIONS

SEE PROFILE

Visualization and characterization of individual type III protein secretion machines in live bacteria

Yongdeng Zhang (章永登)[a,1], María Lara-Tejero[b,1], Jörg Bewersdorf[a,c,2], and Jorge E. Galán[b,2]

[a]Department of Cell Biology, School of Medicine, Yale University, New Haven, CT 06520; [b]Department of Microbial Pathogenesis, School of Medicine, Yale University, New Haven, CT 06536; and [c]Department of Biomedical Engineering, School of Medicine, Yale University, New Haven, CT 06520

Contributed by Jorge E. Galán, May 4, 2017 (sent for review April 7, 2017; reviewed by Hans Wolf-Watz and Xiaowei Zhuang)

Type III protein secretion machines have evolved to deliver bacterially encoded effector proteins into eukaryotic cells. Although electron microscopy has provided a detailed view of these machines in isolation or fixed samples, little is known about their organization in live bacteria. Here we report the visualization and characterization of the *Salmonella* type III secretion machine in live bacteria by 2D and 3D single-molecule switching superresolution microscopy. This approach provided access to transient components of this machine, which previously could not be analyzed. We determined the subcellular distribution of individual machines, the stoichiometry of the different components of this machine in situ, and the spatial distribution of the substrates of this machine before secretion. Furthermore, by visualizing this machine in *Salmonella* mutants we obtained major insights into the machine's assembly. This study bridges a major resolution gap in the visualization of this nanomachine and may serve as a paradigm for the examination of other bacterially encoded molecular machines.

bacterial nanomachines | protein secretion | superresolution microscopy | bacterial pathogenesis | *Salmonella* virulence

Type III secretion systems are remarkable molecular machines with the capacity to inject multiple bacterial proteins into eukaryotic cells (1, 2). These machines play an essential role in the pathogenic or symbiotic relationships between the bacteria that encode them and their respective hosts. Consequently, type III secretion systems are rapidly emerging as targets for the development of novel therapeutic and prevention strategies with the potential to combat several important infectious diseases (3–5). The components of type III secretion machines are highly conserved across bacterial species although the effector proteins that they deliver are customized for the specific bacteria that harbor them (1, 6, 7). The entire type III secretion machine or injectisome is ∼40 nm in width and ∼150 nm in length and is organized in defined substructures (Fig. 1*A*). The best-characterized substructure is the needle complex, which is a multi-ring cylindrical structure embedded in the bacterial envelope with a needle-like extension that projects several nanometers from the bacterial surface. The needle complex is traversed by a narrow channel that serves as the conduit for the proteins that travel this secretion pathway (8). The needle is capped at its end by the tip complex, which is thought to coordinate the activation of the secretion machine upon contact with target cells (9, 10). Because the needle complex can be isolated in a manner suitable for single-particle cryo-electron microscopy, its organization at the quasi-atomic level is known (11–18). Passage of the secreted proteins through the inner membrane requires the export apparatus, which is composed of a group of poly-topic inner membrane proteins located at the center of the needle complex base (19). Finally, several cytoplasmic proteins form a large complex known as the sorting platform that is involved in selecting and sorting the proteins that are destined to travel the type III secretion pathway (20, 21). Because the sorting platform dissociates from the needle complex during isolation, its organization and structure are not as well understood (22–24). Recent cryo-electron tomography studies have provided unique insight into the molecular architecture of the sorting platform although the precise stoichiometry of some of its components is not known (25, 26). Although emphasis has been placed on obtaining the highest possible resolution view of the type III secretion machine and its components, there are important questions that require visualization of individual machines in the context of the entire live bacterium. Attempts have been made to study the organization of the type III secretion system in live bacteria using fluorescently tagged components (27, 28). However, due to the small size of the injectisome, previous approaches have not successfully resolved individual machines within the bacterial cell and therefore have not been able to address critical questions that require this higher level of resolution. The development of superresolution imaging techniques has made possible the visualization of subcellular structures at an unprecedented level of resolution (29, 30). Here we have used 2D (31) and 3D (32) single-molecule switching nanoscopy (SMSN) to visualize the different structural elements of the type III secretion system in live bacteria, providing major insight into the assembly and function of this bacterial nanomachine.

Results and Discussion

Visualization of the *S.* Typhimurium Type III Secretion Needle Complex by Superresolution Microscopy. To visualize the needle complex of the type III secretion injectisome of *Salmonella enterica* serovar Typhimurium (*S.* Typhimurium) (8) by SMSN, we first constructed a strain expressing PrgH, a component of its inner ring (18) (Fig. 1*A* and *SI Appendix*, Fig. S1*A*), fused at its

Significance

Type III protein secretion systems are essential virulence factors for many bacterial pathogens. Cryo-electron microscopy has provided important details about the architecture and molecular organization of the type III secretion machine in isolation or in fixed samples. However, little information is available about the organization of the type III secretion machine and its individual substructures in live bacteria. Using 2D and 3D single-molecule switching superresolution microscopy, we have visualized individual type III secretion machines in live bacteria and obtained unique insight into the assembly and function of these machines. These studies bridge a major resolution gap in the visualization of type III secretion machines and may serve as a paradigm for the examination of other bacterially encoded molecular machines.

Author contributions: Y.Z., M.L.-T., J.B., and J.E.G. designed research; Y.Z. and M.L.-T. performed research; Y.Z., M.L.-T., J.B., and J.E.G. analyzed data; and Y.Z., M.L.-T., J.B., and J.E.G. wrote the paper.

Reviewers: H.W.-W., Umea University; and X.Z., Harvard University/Howard Hughes Medical Institute.

Conflict of interest statement: J.B. discloses significant financial interest in Bruker Corp. and Hamamatsu Photonics.

[1]Y.Z. and M.L.-T. contributed equally to this work.

[2]To whom correspondence may be addressed. Email: jorge.galan@yale.edu or joerg.bewersdorf@yale.edu.

This article contains supporting information online at www.pnas.org/lookup/suppl/doi:10.1073/pnas.1705823114/-/DCSupplemental.

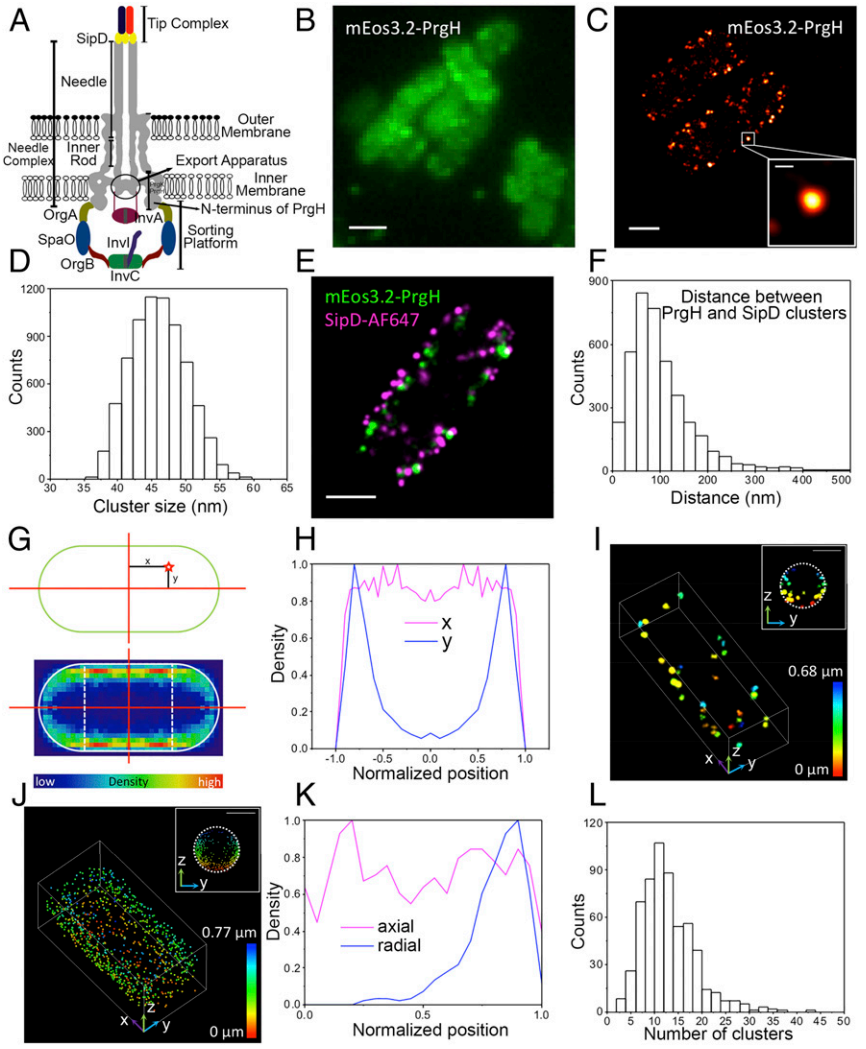

Fig. 1. Visualization of the *S.* Typhimurium type III secretion needle complex by superresolution microscopy. (*A*) Schematic representation of the *S.* Typhimurium type III secretion injectisome. (*B*), Wide-field (imaging mEos3.2 without photoactivation) (*B*) and superresolution (2D) (*C*) images of live *S.* Typhimurium expressing mEos3.2-PrgH. [Scale bar: 1 μm (*B*); 500 nm (*C*); 50 nm (*Inset*, *C*).] (*D*) Distribution of the cluster sizes (mean size 45.98 ± 0.05 nm; 7,295 clusters examined). (*E*) Two-color superresolution image (2D) of fixed *S.* Typhimurium expressing mEos3.2-PrgH stained with an AF647-labeled antibody directed to an epitope tag present in the needle tip protein SipD. (Scale bar: 500 nm.) (*F*) Nearest neighbor distance between the fluorescent clusters associated with PrgH and SipD (mean distance 101 ± 1 nm; 3,976 clusters measured). (*G*) A 2D histogram of all clusters from all bacteria. The position of each cluster was normalized to the cell dimensions (see diagram), and clusters were placed on the first quadrant of the cell and mirrored to the other quadrants. (*H*) Normalized cluster density along the *x* and *y* axes. Only localizations within the dashed region in *G* were used for the calculation of the density along the *y* axis to eliminate the effect of the reduced radius at the bacterial poles. (*I*) 4Pi-SMSN image (3D) of mEos3.2-PrgH. (*J*) The 3D distribution of PrgH clusters accumulated from 58 bacteria cells. Each dot represents the center position of a cluster. *Inset* images (3D) in *I* and *J* show the *y*–*z* view of the clusters within the center half of the cell. (Scale bar: 500 nm.) (*K*) Normalized cluster density along the axial (*x*) and radial (*y*–*z* plane) directions of the clusters shown in *J*. Only clusters within the center half of the cells were used for the calculations of the cluster density along the radial direction. (*L*) Number of mEos3.2-PrgH clusters observed in live bacteria (mean number per bacteria 12.5 ± 0.7; 585 bacterial cells analyzed).

cytoplasmic amino terminus to the photoactivatable fluorescent protein mEos3.2 (33). We chose this component because its topological organization, size, and stoichiometry are known, thus allowing the precise calibration of the image analysis algorithms (Fig. 1*A* and *SI Appendix*, Fig. S1). Furthermore, the imaging of PrgH provided a feasibility test for the experimental approach. We constructed the bacterial strain so that expression of the fusion protein was directed from the appropriate chromosomal context to ensure wild-type levels of expression. Furthermore, we verified that the fusion protein maintained wild-type function, that it was efficiently incorporated into fully assembled needle complexes, and, importantly, that the fluorescent tag was not cleaved from the tagged protein (*SI Appendix*, Fig. S2). We grew the mEos3.2-PrgH–expressing bacteria under conditions that stimulate the expression of the type III secretion system and imaged them by SMSN (32, 34). Superresolution images of these live bacteria showed the appearance of fluorescent clusters with a diameter of ∼45 nm (Fig. 1 *B*–*D* and *SI Appendix*, Table S1), a measure that, in the context of the estimated resolution of our microscopy (∼35 nm, *SI Appendix*, Fig. S1), is largely consistent with the actual diameter (∼25 nm) of the inner ring of the needle complex (15) (*SI Appendix*, Fig. S1*A*). To confirm that the mEos3.2-PrgH–associated clusters represented needle complexes, we fluorescently labeled the needle tip protein SipD in the bacterial strain expressing mEos3.2-PrgH and simultaneously imaged the two proteins by two-color SMSN in fixed samples (Fig. 1*E*). We found that the average distance between SipD and the PrgH-associated clusters (∼101 nm) (Fig. 1*F*) was consistent with the expected distance between the tip of the needle and the inner ring of the needle complex (∼100 nm) (16), which further supports the notion that the PrgH clusters represent fully assembled needle complexes. The broad distribution of the observed distances reflect the fact that the measurements were carried out after 2D imaging and therefore are influenced by the spatial orientation of the type III secretion machines. We also examined the subcellular distribution of the PrgH-associated fluorescence along both the length (*x*) and width (*y*) of the bacteria. We found that the vast majority of the observed fluorescent clusters were located at the periphery of the bacterial cells (Fig. 1 *G* and *H*), which is consistent with the membrane localization of the needle complex. Although conventional 3D nanoscopy techniques achieve very high resolution in the focal (*x*–*y*) plane, these approaches are more limited in resolution in the axial (*z*) direction (35–37). Therefore, we applied the recently developed whole-cell 4Pi-SMSN (32), which achieves an isotropic superresolution of 20 nm and below in all three dimensions and therefore can provide more accurate volumetric information about the distribution of the type III secretion machines within bacterial cells. We observed that the PrgH-associated fluorescent clusters were distributed throughout the bacterial periphery with very little signal detected within the bacterial cytoplasm (Fig. 1 *I*–*K* and Movie S1). For reference, we also imaged *S.* Typhimurium that

displayed the fluorescently labeled needle tip protein SipD with 4Pi-SMSN and determined that ~93% of the PrgH-associated fluorescent clusters were located at the periphery of the bacterial cells (as defined by the SipD staining; *SI Appendix*, Fig. S3 and Movie S1). Taken together, these observations confirm that the PrgH-associated fluorescent clusters represent assembled needle complexes on the bacterial envelope and that the imaging approach can resolve single type III secretion injectisomes.

Distribution of the Type III Secretion Machines in Live Bacteria. It is often the case that bacterial nanomachines are assembled at specific sites within the bacterial envelope (38–40). For example, some bacteria deploy their flagellar or type IV protein secretion machines at their poles, and many bacteria deploy components of their cell division machine at the midplate (41–43). Although needle complexes can be visualized by electron microscopy at the bacterial envelope (8), this approach is not amenable for a comprehensive analysis of the distribution of the type III secretion machines throughout the bacterial cell, nor can it easily provide an accurate measure of the number of machines present in each bacterium. The ability to visualize individual needle complexes in many live bacteria allowed us to determine their distribution within the bacterial body and to obtain an estimate of the number of type III secretion machines present in *S.* Typhimurium. Analysis of the PrgH-associated clusters indicated that the needle complexes are randomly distributed throughout the bacterial envelope (Fig. 1 *C* and *E* and *SI Appendix*, Figs. S3 and S4). We also observed variability in the number of PrgH-associated fluorescent clusters present in each individual bacterial cell (Fig. 1*L* and *SI Appendix*, Table S1). The molecular basis for this cell-to-cell variability is unknown, but the wide distribution suggests the existence of yet undiscovered stochastic regulatory mechanisms controlling the expression of the type III secretion system. The actual number of needle complexes, however, is likely to be higher as some clusters may be away from the focal plane and may escape detection. In addition, cluster detection would require the imaging of a minimum number of photon-switching events (five in our case), and although there are 24 mEos3.2-PrgH molecules in each needle complex that could be potentially imaged, it is likely that some needle complexes may not reach the minimum detection threshold because it has been reported that only 42% of mEos3.2 can be photoactivated to a fluorescently detectable form (44).

Visualization of the Type III Secretion Sorting Platform. Although the composition and stoichiometry of the needle complex components are known (16, 18, 45), less information is available regarding the cytoplasmic sorting platform, and the inability to isolate this substructure has hampered efforts to determine its stoichiometry (20). To gain insights into the sorting platform, we constructed a *S.* Typhimurium strain that expresses a core component of this substructure, SpaO, tagged with mEos3.2 from its native chromosomal context. We found that the function of the tagged SpaO was indistinguishable from wild type and,

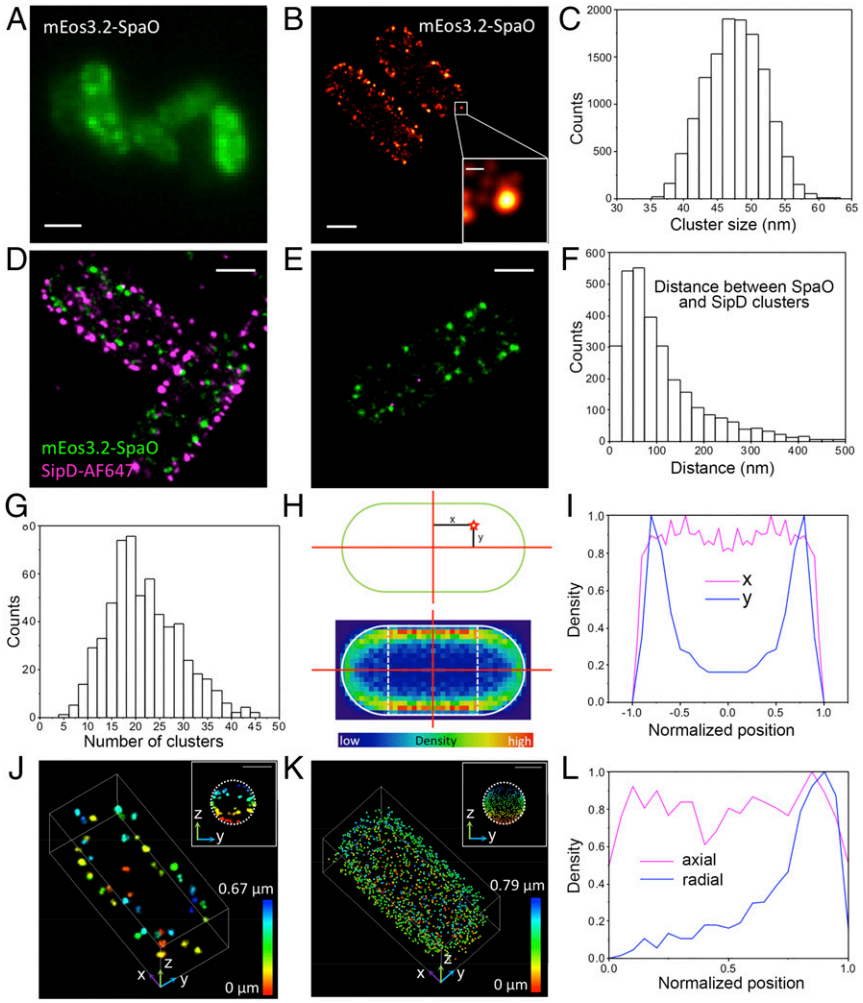

Fig. 2. Visualization of the type III secretion sorting platform by superresolution microscopy. (*A* and *B*) Wide-field (*A*) and superresolution (2D) (*B*) images of live *S.* Typhimurium expressing mEos3.2-SpaO. [Scale bar: 1 μm (*A*); 500 nm (*B*); 50 nm (*Inset*, *B*)]. (*C*) Distribution of the cluster sizes (measured as full width at half-maxima) (mean size 47.58 ± 0.04 nm of 12,710 clusters examined). (*D* and *E*) Two-color superresolution image (2D) of fixed *S.* Typhimurium expressing mEos3.2-SpaO stained with an AF647-labeled antibody directed to an epitope tag present in the type III secretion needle tip protein SipD. An image (2D) of an identically processed control sample of *S.* Typhimurium expressing a nontagged SipD protein is shown in *E*. (Scale bar: 500 nm.) (*F*) Distance between the fluorescent clusters associated with SpaO and SipD (mean distance 106 ± 2 nm; 2,952 clusters measured). (*G*) Number of mEos3.2-SpaO clusters observed in live bacteria (mean number per bacteria 21.4 ± 0.3; 595 bacterial cells analyzed). (*H*) A 2D histogram of clusters (bin cluster positions from all bacteria as described for PrgH). (*I*) Normalized cluster density along the *x* and *y* axes. Only localizations within the dashed region in *H* (half length of the cell) were used for the calculation of the density along the *y* axis to exclude the localizations from the bacterial poles. (*J*) 4Pi-SMSN image (3D) of *S.* Typhimurium expressing mEos3.2-SpaO. (*K*) The 3D distribution of SpaO clusters from 65 bacteria cells. Each dot represents the center position of a cluster. *Inset* images in *J* and *K* show the *y*–*z* view of the clusters within the center half of the cell. (Scale bar: 500 nm.) (*L*) Normalized cluster density along the axial (*x*) and radial (*y*–*z* plane) direction of the clusters shown in *K*. Only clusters within the center half of the cell were used for the calculation of the cluster density along the radial direction.

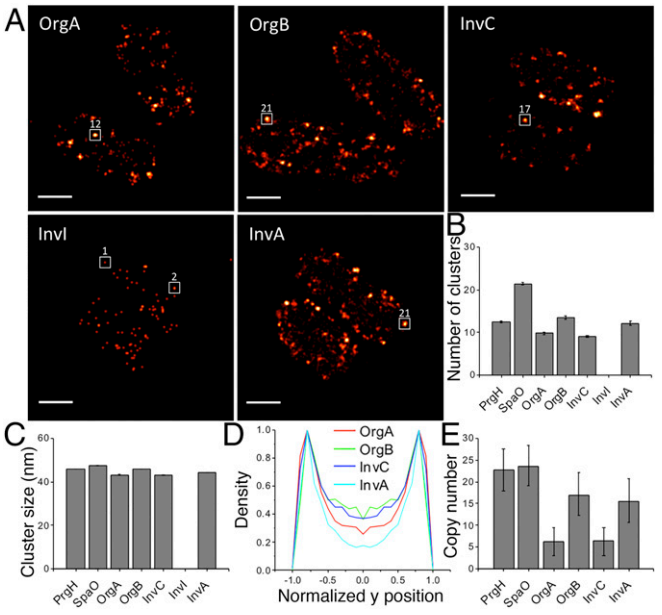

Fig. 3. Visualization and stoichiometry of type III secretion sorting platform and export apparatus components by superresolution microscopy. (*A*) Superresolution images (2D) of live *S.* Typhimurium expressing the mEos3.2-tagged sorting platform components OrgA, OrgB, InvC, or InvI and the export apparatus component InvA. All images are adjusted for optimal contrast. Numbers above the white boxes indicate the number of localizations within the indicated areas in each image. InvI contains primarily individual localizations. (Scale bar: 500 nm.) (*B*) Number of fluorescent clusters observed in the indicated live bacterial strains. (*C*) Size of the fluorescent clusters associated with the indicated proteins. (*D*) Normalized cluster density along the *y* axis in the indicated bacteria. (*E*) Estimated number of molecules per cluster in the indicated bacterial strains. Numbers represent the mean ± SE (*B* and *C*) or the mean ± SD (*E*) and are derived from the analysis of between 237 and 642 cells per bacterial strain (*SI Appendix*, Table S1).

importantly, that the chimeric protein was stable, thus ensuring that the fluorescent signal originates only from the tagged protein (*SI Appendix*, Fig. S2). We imaged this strain by SMSN and, similar to PrgH, we found that SpaO appears in clusters with a diameter (~48 nm) consistent with what would be expected for a fully assembled sorting platform (Fig. 2 *A–C* and *SI Appendix*, Table S1). To confirm that these clusters represented bona-fide sorting platforms, we examined their colocalization with the fluorescently labeled needle tip protein SipD in fixed samples by two-color SMSN (Fig. 2 *D* and *E*). We found that the average distance between the SipD- and SpaO-associated signals (~105 nm) (Fig. 2*F*) was consistent with the predicted distance between the tip of the needle and the cytoplasmic sorting platform (~110 nm), even though, as discussed above, these 2D measurements are affected by the geometry and spatial orientation of the type III secretion machines. These results therefore indicate that the majority of the SpaO clusters, although not all, represent fully assembled sorting platforms. We examined the number of the SpaO-associated clusters (Fig. 2*G* and *SI Appendix*, Table S1) and their distribution along the *x* and *y* axes (Fig. 2 *H* and *I*) within the bacterial body. We found a higher number of SpaO-associated clusters than those associated with PrgH, suggesting that some SpaO complexes (i.e., either partially or fully assembled sorting platforms) are not associated with needle complexes. Consistent with this hypothesis, a higher number of the SpaO clusters were located away from the bacterial membrane (Fig. 2 *H* and *I*) than in the case of PrgH. We corroborated this observation by whole-cell 4Pi-SMSN, which showed ~20% of the SpaO-associated fluorescent clusters within the bacterial cytoplasm (Fig. 2 *J–L*; *SI Appendix*, Fig. S3; Movie S1). These observations are consistent with previous biochemical data indicating that a significant proportion of SpaO is not associated with the needle complex (20) and suggest that, as previously proposed (20, 28), this structure might be dynamic.

Stoichiometry of Sorting-Platform Components Determined by Superresolution Microscopy. In addition to SpaO, four additional proteins, OrgA, OrgB, InvC, and InvI, are thought to form the sorting platform (20). However, the relative stoichiometry of these components has not been determined due to the inability to isolate this complete substructure. We constructed *S.* Typhimurium strains encoding functional fusions of each one of the sorting-platform components to mEos3.2, which were placed in the appropriate chromosomal context to ensure wild-type levels of expression (*SI Appendix*, Fig. S5). We also constructed a strain expressing a functional mEos3.2 fusion to the cytoplasmic domain of InvA, a component of the export apparatus (19) (*SI Appendix*, Fig. S5). Superresolution microscopy visualization of the resulting strains showed the presence of OrgA-, OrgB-, InvC-, and InvA-associated clusters that were similar in number, size, and distribution to those observed for SpaO (Fig. 3 *A–D* and *SI Appendix*, Table S1). No clusters associated with InvI were observed (Fig. 3 *A* and *B*), which is consistent with data on InvI's flagellar homologs, which are thought to be present in only one copy per flagella (46). Like SpaO, a number of the OrgA-, OrgB-, and InvC-associated clusters were located away from the bacterial membrane (Fig. 3*D*), which is consistent with the presence of a small fraction of fully or partially assembled sorting platforms

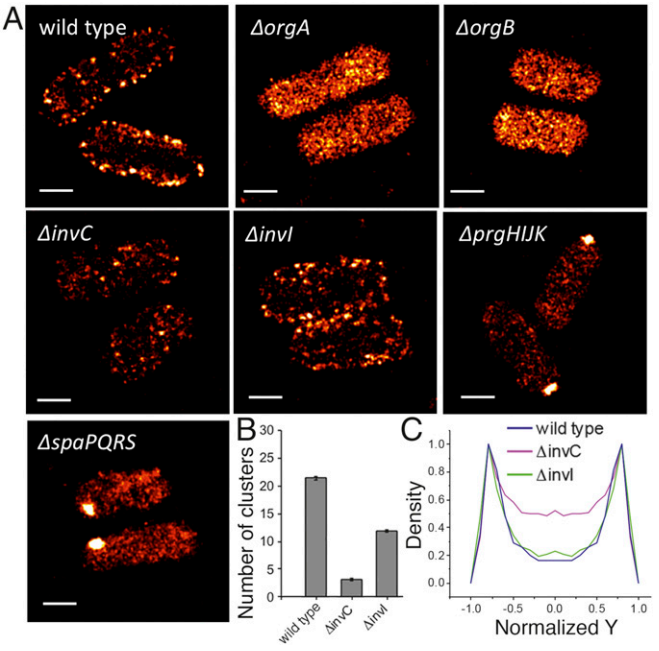

Fig. 4. Examination of the sorting-platform assembly and effector protein localization by superresolution microscopy. (*A*) Effect of the absence of sorting platform, export apparatus, or needle complex components on the localization of the sorting-platform core component SpaO. Shown are superresolution images (2D) of wild-type *S.* Typhimurium or the indicated deletion mutant strains expressing mEos3.2-SpaO. (Scale bar: 500 nm.) (*B*) Number of fluorescent clusters observed in the indicated live bacterial strains. Numbers represent the mean ± SE (mean numbers: wild type, 21.4 ± 0.3; Δ*invC*, 3.1 ± 0.1; Δ*invI*, 11.8 ± 0.2). (*C*) Normalized SpaO-mEos3.2 fluorescent cluster density along *y* axis in the indicated live bacterial strains. Clusters were not detected in the other strains. When clusters were present, at least 595 bacterial cells were analyzed (*SI Appendix*, Table S1).

that are not associated with the needle complex. In contrast, the InvA-associated clusters were all found at the cell periphery (Fig. 3*D*), which is consistent with its membrane localization. To estimate the stoichiometry of the sorting-platform components, we performed a simulation that allowed us to correct the observed copy numbers per cluster for photophysical effects and a bias of our cluster-finding algorithm (*SI Appendix*, Fig. S6). Our results suggest that SpaO is present in an approximately stoichiometric relationship with PrgH, whereas OrgA, OrgB, InvC, and InvA are present in substoichiometric amounts (Fig. 3*E* and *SI Appendix*, Fig. S6 and Table S1). The inability to observe clusters associated with InvI prevented the determination of its stoichiometry but suggests that this protein must be present in much lower numbers within each sorting platform, which is consistent with previous reports (46). Taken together, these results have provided the localization and relative stoichiometry of components of the sorting platform and export apparatus in situ in the context of fully assembled injectisomes.

Examination of the Sorting Platform Assembly. To gain insights into the assembly of the sorting platform, we examined by SMSN the effect of mutations in different sorting-platform components on the localization of SpaO, a core component of this injectisome substructure. We found that, in the absence of OrgA or OrgB, the SpaO clusters disappeared and the fluorescent signal became evenly distributed throughout the bacterial cytosol (Fig. 4 *A* and *B* and *SI Appendix*, Table S1) even though there was no detectable cleavage of the fusion protein (*SI Appendix*, Fig. S7). In contrast, the absence of InvI and InvC reduced but did not eliminate the formation of mEos3.2-SpaO–associated clusters (Fig. 4 *A* and *B*), although in the case of the *ΔinvC* mutant a significant proportion of the observed clusters were located away from the cell periphery (Fig. 4*C*). These results indicate that OrgA, OrgB, and SpaO are the core components of the sorting platform and must presumably interact with one another to form a stable structure to which InvC and InvI may be later recruited, resulting in the overall stabilization of the fully assembled sorting platform. It has been proposed that the sorting platform associates with the needle complex by interactions with its cytoplasmic inner ring (20). To explore the role of the needle complex in the assembly of the sorting platform, we examined the localization of SpaO in a *S.* Typhimurium mutant strain (Δ*prgH*Δ*prgI*Δ*prgJ*Δ*prgK*) that lacks the needle complex substructure. We found that, in the absence of the needle complex, SpaO was no longer organized in peripheral or cytoplasmic clusters (Fig. 4 *A* and *B* and *SI Appendix*, Table S1). Instead, SpaO localized in large aggregates at one of the poles of the bacterial cell (Fig. 4*A*), an observation corroborated by confocal fluorescence microscopy using GFP instead of mEos3.2 as a fluorescent marker (*SI Appendix*, Fig. S8). These results indicate that an intact needle complex is necessary to coordinate the assembly of the sorting platform and that, in its absence, the sorting-platform components may engage in aberrant interactions leading to their mislocalization to the bacterial poles. We made similar observations in a *S.* Typhimurium mutant strain (Δ*spaP*Δ*spaQ*Δ*spaR*Δ*spaS*) lacking the export apparatus components (Fig. 4*A* and *SI Appendix*, Fig. S8), which results in a drastically reduced number of assembled needle complexes (19). Taken together, these results indicate that the assembly of the needle complex must precede the assembly of the sorting platform and that SpaO, OrgA, and OrgB are the central components of the sorting platform.

Visualization of Effector Protein Localization in Live Bacteria. Upon activation of the type III secretion machine, presumably after contact with its target cells, protein secretion and translocation are thought to occur very rapidly (47). Therefore, before secretion, effector proteins are likely to be queued at a privilege site so that they can be rapidly engaged by the secretion machine.

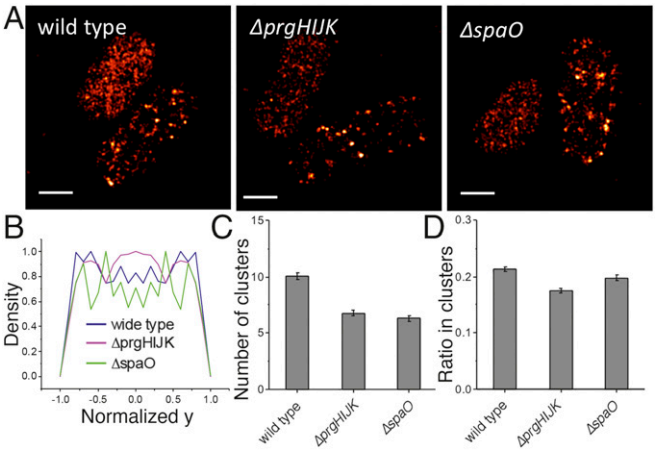

Fig. 5. Localization of effector proteins in live bacteria. (*A*) Localization of the effector protein SopB in live bacteria. Shown are superresolution images (2D) of wild-type *S.* Typhimurium or the indicated deletion mutant strains expressing SopB-mEos3.2. (Scale bar: 500 nm.) (*B*) Normalized SopB-mEos3.2 fluorescent cluster density along the *y* axis in the indicated live bacterial strains. At least 543 bacteria per indicated strain were analyzed (*SI Appendix*, Table S1). (*C*) Number of SopB-mEos3.2 fluorescent clusters observed in the indicated live bacterial strains. Numbers represent the mean ± SE of a minimum of 543 cells analyzed per bacterial strains (*SI Appendix*, Table S1). (*D*) Ratio of total SopB-mEos3.2–associated fluorescence visualized in clusters. Numbers are the mean ± SE of the indicated strains. In each case, at least 543 bacteria were analyzed.

When grown in regular culture medium, type III secretion machines are largely inactive (<10% of the pool of type III secreted protein can be found in the culture supernatant) (48, 49) but poised for activation because they readily translocate proteins into target cells upon infection (47). We took advantage of this observation to investigate the location of effector proteins within the bacterial cell before secretion. We constructed a strain expressing a fusion of mEos3.2 to SopB, an effector protein known to be among the first to be translocated to target cells (50). We found that a significant proportion of the fluorescence associated with SopB was arranged in large clusters, which varied in number (Fig. 5*A* and *SI Appendix*, Table S1). However, unlike the clusters associated with the needle complex and sorting-platform components, which were largely seen at the periphery of the bacteria, the SopB-associated clusters were located within the bacterial cytoplasm, indicating that they are not associated with the fully assembled injectisomes (Fig. 5*B*). Consistent with this notion, the arrangement, number, and distribution of the SopB clusters did not change in the absence of the needle complex or the sorting-platform components (Fig. 5 *C* and *D* and *SI Appendix*, Table S1). These results indicate that a significant proportion of the effector proteins are arranged in large, mostly immobile, complexes within the bacterial cytoplasm but not in association with the injectisome. Although the functional implications and biochemical organization of these effector protein-associated clusters remain to be determined, these observations suggest the existence of a subcellular compartment where these proteins await the secretion-activating signal.

Conclusions. We have used 2D and 3D SMSN to visualize the type III secretion machine in live bacteria in *S.* Typhimurium at an unprecedented level of detail, thus providing major insights into its structure and assembly. The highly conserved nature of this machine indicates that these findings are likely to apply to homologous machines encoded by other important pathogens. Additionally, the detailed knowledge of the organization and molecular composition of some components of the type III protein secretion

machine offer a unique biological calibration standard for future quantitative superresolution studies. Therefore, these studies not only may help the development of novel therapeutic strategies to combat important infectious disease but also provide a template for the study of other bacterial nanomachines.

Materials and Methods

S. Typhimurium strains are listed in *SI Appendix*, Table S1, and were grown to maximize expression of the type III secretion system (51). Analysis of type III protein secretion function was carried out as previously described (52). For SMSN or 4Pi-SMSN, bacteria were placed on agarose pads or on poly-D-lysine–coated glass-bottom microwell dishes, respectively. The 2D and 3D superresolution imaging was performed with a custom-built FPALM system as previously described (31, 32, 34, 53). Cluster analysis was carried out using a DBSCAN clustering algorithm (54, 55) and a wavelet algorithm (56) as described in *SI Appendix, Materials and Methods*. The copy number of sorting-platform components was derived from the cluster analysis as detailed in *SI Appendix, Materials and Methods*. More detailed methods and any associated references are available in *SI Appendix, Materials and Methods*.

ACKNOWLEDGMENTS. We thank Hesper Rego and members of the Galán laboratory for critical reading of the manuscript. This work was supported by National Institute of Allergy and Infectious Diseases Grant AI030492 (to J.E.G.); National Institute of Diabetes and Digestive and Kidney Diseases Grant P30 DK45735; and Wellcome Trust Grant 095927/A/11/Z (to J.B.).

1. Galán JE, Lara-Tejero M, Marlovits TC, Wagner S (2014) Bacterial type III secretion systems: Specialized nanomachines for protein delivery into target cells. *Annu Rev Microbiol* 68:415–438.
2. Cornelis GR (2010) The type III secretion injectisome, a complex nanomachine for intracellular 'toxin' delivery. *Biol Chem* 391:745–751.
3. Gu L, Zhou S, Zhu L, Liang C, Chen X (2015) Small-molecule inhibitors of the type III secretion system. *Molecules* 20:17659–17674.
4. Charro N, Mota LJ (2015) Approaches targeting the type III secretion system to treat or prevent bacterial infections. *Expert Opin Drug Discov* 10:373–387.
5. Tsou LK, et al. (2016) Antibacterial flavonoids from medicinal plants covalently inactivate type III protein secretion substrates. *J Am Chem Soc* 138:2209–2218.
6. Galán JE (2009) Common themes in the design and function of bacterial effectors. *Cell Host Microbe* 5:571–579.
7. Galán JE (2007) SnapShot: Effector proteins of type III secretion systems. *Cell* 130:192.
8. Kubori T, et al. (1998) Supramolecular structure of the *Salmonella typhimurium* type III protein secretion system. *Science* 280:602–605.
9. Mueller CA, Broz P, Cornelis GR (2008) The type III secretion system tip complex and translocon. *Mol Microbiol* 68:1085–1095.
10. Wang Y, Zhang L, Picking WL, Picking WD, De Guzman RN (2008) Structural dissection of the extracellular moieties of the type III secretion apparatus. *Mol Biosyst* 4:1176–1180.
11. Burkinshaw BJ, Strynadka NC (2014) Assembly and structure of the T3SS. *Biochim Biophys Acta* 1843:1649–1663.
12. Kosarewicz A, Königsmaier L, Marlovits TC (2012) The blueprint of the type-3 injectisome. *Philos Trans R Soc Lond B Biol Sci* 367:1140–1154.
13. Chatterjee S, Chaudhury S, McShan AC, Kaur K, De Guzman RN (2013) Structure and biophysics of type III secretion in bacteria. *Biochemistry* 52:2508–2517.
14. Erhardt M, Namba K, Hughes KT (2010) Bacterial nanomachines: The flagellum and type III injectisome. *Cold Spring Harb Perspect Biol* 2:a000299.
15. Marlovits TC, et al. (2004) Structural insights into the assembly of the type III secretion needle complex. *Science* 306:1040–1042.
16. Marlovits TC, et al. (2006) Assembly of the inner rod determines needle length in the type III secretion injectisome. *Nature* 441:637–640.
17. Schraidt O, Marlovits TC (2011) Three-dimensional model of Salmonella's needle complex at subnanometer resolution. *Science* 331:1192–1195.
18. Schraidt O, et al. (2010) Topology and organization of the Salmonella typhimurium type III secretion needle complex components. *PLoS Pathog* 6:e1000824.
19. Wagner S, et al. (2010) Organization and coordinated assembly of the type III secretion export apparatus. *Proc Natl Acad Sci USA* 107:17745–17750.
20. Lara-Tejero M, Kato J, Wagner S, Liu X, Galán JE (2011) A sorting platform determines the order of protein secretion in bacterial type III systems. *Science* 331:1188–1191.
21. Notti RQ, Bhattacharya S, Lilic M, Stebbins CE (2015) A common assembly module in injectisome and flagellar type III secretion sorting platforms. *Nat Commun* 6:7125–7133.
22. Kudryashev M, et al. (2013) In situ structural analysis of the Yersinia enterocolitica injectisome. *eLife* 2:e00792.
23. Kawamoto A, et al. (2013) Common and distinct structural features of Salmonella injectisome and flagellar basal body. *Sci Rep* 3:3369.
24. Nans A, Kudryashev M, Saibil HR, Hayward RD (2015) Structure of a bacterial type III secretion system in contact with a host membrane in situ. *Nat Commun* 6:10114.
25. Hu B, et al. (2015) Visualization of the type III secretion sorting platform of Shigella flexneri. *Proc Natl Acad Sci USA* 112:1047–1052.
26. Hu B, Lara-Tejero M, Kong Q, Galán JE, Liu J (2017) In situ molecular architecture of the Salmonella type III secretion machine. *Cell* 168:1065–1074.e10.
27. Diepold A, et al. (2010) Deciphering the assembly of the Yersinia type III secretion injectisome. *EMBO J* 29:1928–1940.
28. Diepold A, Kudryashev M, Delalez NJ, Berry RM, Armitage JP (2015) Composition, formation, and regulation of the cytosolic c-ring, a dynamic component of the type III secretion injectisome. *PLoS Biol* 13:e1002039.
29. Hell S, et al. (2015) The 2015 super-resolution microscopy roadmap. *J Phys D Appl Phys* 48:1–34.
30. Tuson HH, Biteen JS (2015) Unveiling the inner workings of live bacteria using super-resolution microscopy. *Anal Chem* 87:42–63.
31. Huang F, et al. (2013) Video-rate nanoscopy using sCMOS camera-specific single-molecule localization algorithms. *Nat Methods* 10:653–658.
32. Huang F, et al. (2016) Ultra-high resolution 3D imaging of whole cells. *Cell* 166:1028–1040.
33. Zhang M, et al. (2012) Rational design of true monomeric and bright photoactivatable fluorescent proteins. *Nat Methods* 9:727–729.
34. Laplante C, Huang F, Tebbs IR, Bewersdorf J, Pollard TD (2016) Molecular organization of cytokinesis nodes and contractile rings by super-resolution fluorescence microscopy of live fission yeast. *Proc Natl Acad Sci USA* 113:E5876–E5885.
35. Juette MF, et al. (2008) Three-dimensional sub-100 nm resolution fluorescence microscopy of thick samples. *Nat Methods* 5:527–529.
36. Pavani SR, et al. (2009) Three-dimensional, single-molecule fluorescence imaging beyond the diffraction limit by using a double-helix point spread function. *Proc Natl Acad Sci USA* 106:2995–2999.
37. Huang B, Wang W, Bates M, Zhuang X (2008) Three-dimensional super-resolution imaging by stochastic optical reconstruction microscopy. *Science* 319:810–813.
38. Costa TR, et al. (2015) Secretion systems in Gram-negative bacteria: Structural and mechanistic insights. *Nat Rev Microbiol* 13:343–359.
39. Yao Z, Carballido-López R (2014) Fluorescence imaging for bacterial cell biology: From localization to dynamics, from ensembles to single molecules. *Annu Rev Microbiol* 68:459–476.
40. Coltharp C, Xiao J (2012) Superresolution microscopy for microbiology. *Cell Microbiol* 14:1808–1818.
41. Kazmierczak BI, Hendrixson DR (2013) Spatial and numerical regulation of flagellar biosynthesis in polarly flagellated bacteria. *Mol Microbiol* 88:655–663.
42. Christie PJ, Atmakuri K, Krishnamoorthy V, Jakubowski S, Cascales E (2005) Biogenesis, architecture, and function of bacterial type IV secretion systems. *Annu Rev Microbiol* 59:451–485.
43. Haeusser DP, Margolin W (2016) Splitsville: Structural and functional insights into the dynamic bacterial Z ring. *Nat Rev Microbiol* 14:305–319.
44. Durisic N, Laparra-Cuervo L, Sandoval-Álvarez A, Borbely JS, Lakadamyali M (2014) Single-molecule evaluation of fluorescent protein photoactivation efficiency using an in vivo nanotemplate. *Nat Methods* 11:156–162.
45. Zilkenat S, et al. (2016) Determination of the stoichiometry of the complete bacterial type III secretion needle complex using a combined quantitative proteomic approach. *Mol Cell Proteomics* 15:1598–1609.
46. Ibuki T, et al. (2011) Common architecture of the flagellar type III protein export apparatus and F- and V-type ATPases. *Nat Struct Mol Biol* 18:277–282.
47. Schlumberger MC, et al. (2005) Real-time imaging of type III secretion: Salmonella SipA injection into host cells. *Proc Natl Acad Sci USA* 102:12548–12553.
48. Kaniga K, Tucker S, Trollinger D, Galán JE (1995) Homologs of the Shigella IpaB and IpaC invasins are required for Salmonella typhimurium entry into cultured epithelial cells. *J Bacteriol* 177:3965–3971.
49. Collazo CM, Galán JE (1997) The invasion-associated type III system of *Salmonella typhimurium* directs the translocation of Sip proteins into the host cell. *Mol Microbiol* 24:747–756.
50. Zhou D, Chen LM, Hernandez L, Shears SB, Galán JE (2001) A Salmonella inositol polyphosphatase acts in conjunction with other bacterial effectors to promote host cell actin cytoskeleton rearrangements and bacterial internalization. *Mol Microbiol* 39:248–259.
51. Galán JE, Curtiss R, III (1990) Expression of *Salmonella typhimurium* genes required for invasion is regulated by changes in DNA supercoiling. *Infect Immun* 58:1879–1885.
52. Kato J, Lefebre M, Galán JE (2015) Structural features reminiscent of ATP-driven protein translocases are essential for the function of a type III secretion-associated ATPase. *J Bacteriol* 197:3007–3014.
53. Del Viso F, et al. (2016) Congenital heart disease genetics uncovers context-dependent organization and function of nucleoporins at cilia. *Dev Cell* 38:478–492.
54. Shivanandan A, Unnikrishnan J, Radenovic A (2015) Accounting for limited detection efficiency and localization precision in cluster analysis in single molecule localization microscopy. *PLoS One* 10:e0118767.
55. Ester M, Kriegel H-P, Sander J, Xu X (1996) A density-based algorithm for discovering clusters in large spatial databases with noise. *Proceedings of the Second International Conference on Knowledge Discovery and Data Mining (KDD-96)* (AAAI Press, Menlo Park, CA), pp 226–231.
56. Olivo-Marin JC (2002) Extraction of spots in biological images using multiscale products. *Pattern Recognit* 35:1989–1996.

Supporting Information

Zhang et al. 10.1073/pnas.1705823114

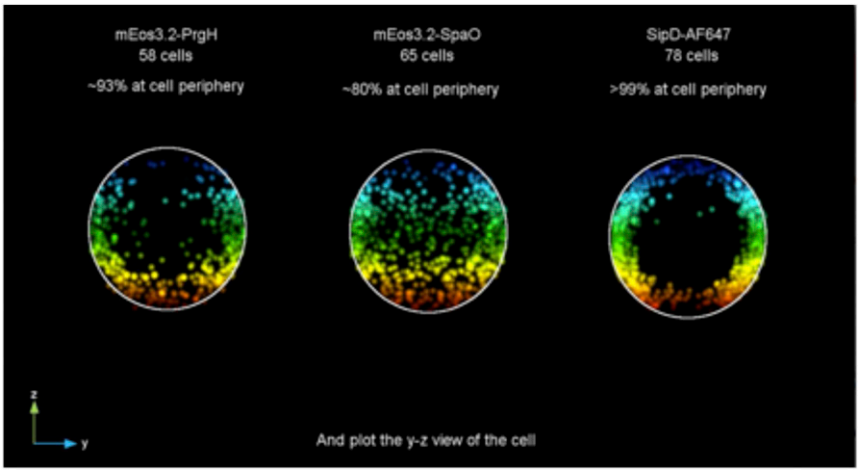

Movie S1. The 4Pi-SMSN imaging of the *S.* Typhimurium type III secretion injectisome. The 4Pi-SMSN images of mEos3.2-PrgH, mEos3.2-SpaO, and SipD-AF647 are shown. After 3D cluster analysis, the center position of each cluster was localized and normalized according to the length and diameter of each bacteria cell. The 3D distribution of the center positions of the clusters associated with each protein combined from multiple cells are shown, and the percentage located at the cell periphery is noted.

Movie S1

Other Supporting Information Files

SI Appendix (PDF)

Supplementary Materials

Visualization and characterization of individual type III protein secretion machines in live bacteria

Yongdeng Zhang[1*], Maria Lara-Tejero[2*], Joerg Bewersdorf[1,3,§], Jorge E. Galán[2§]

[1]Department of Cell Biology, [2]Department of Microbial Pathogenesis, and Department of Biomedical Engineering, School of Medicine, Yale University, New Haven, CT 06536, USA

This PDF file includes:

Supplementary Methods

Supplementary Figs. S1 to S8

Supplementary Tables S1 and S2

Materials and Methods

Bacterial strains and plasmids

All bacterial strains used in this study are derived from *Salmonella enterica* serovar Typhimurium strain SL1344 (1) and are listed in Supplementary Table S2. All strains were constructed by standard recombinant DNA and allelic exchange procedures as previously described (2).

Analysis of type III protein secretion function

The functionality of the type III secretion system in the different *S.* Typhimurium strains was tested by examining their ability to secrete type III secreted proteins to the culture supernatant. Briefly, overnight cultures of the specific strains were diluted 1/20 into LB containing 0.3M NaCl to induce the expression of SPI-1 T3SS (3). Diluted cultures were grown at 37ºC on a rotating wheel to an OD600 of ~ 0.9 (4 to 5 hours) and then the cells were pelleted by centrifugation at 6,000 rpm. The cell pellet was resuspended in 1X SDS-running buffer at 10X concentration so that 10 µl of the resuspension equaled 100 µl of cells. The culture supernatants were filtered through a 0.45 µm syringe filter and proteins in the supernatant were recovered by trichloroacetic acid (TCA) precipitation. The protein precipitate was resuspended in 1x SDS-running buffer and run on a 10% SDS-PAGE gel for Western blot analysis with antibodies against the type III secreted proteins SipB, SipC and InvJ.

Bacterial growth and sample preparation for super-resolution microscopy analysis

Bacteria were grown in 0.3 M NaCl and ampicillin containing LB and 0.1% arabinose to induce the expression of *hilA* from plasmid pSB3292 at 37ºC in a rotating wheel to an OD600 ~0.9. One ml of such

culture was pelleted at 6,000 rpm 2.5 min and washed 7 times with 1 ml of filtered pure water. After the last wash the bacterial pellet was resuspended in 100 µl of filtered pure water and 2 µl of such suspension were deposited on top of a 1% agarose pad (prepared with filtered pure water) contained inside an adhesive gene frame (Thermofisher AB0577) on a microscope slide previously washed with 1M KOH. After 2 min incubation to allow the bacteria to settle on the agarose pad, the pad was covered with a 22 x 22 mm glass cover slip (previously washed with 1M KOH) and the samples were imaged immediately after. To prepare samples for two-color super-resolution imaging bacteria expressing either mEos3.2-PrgH or mEos3.2-SpaO and SipD-3xFlag (4) proteins were grown as described above under SPI-1 inducing conditions. Bacterial cells from 1 ml culture were recovered by centrifugation, resuspended in 4% para-formaldehyde and incubated for 20 min at RT for fixation. Bacterial cells were pelleted, washed 2x in 1ml of PBS and resuspended in 250 µl of PBS containing 3% BSA. After 20 min incubation, anti-FLAG M2 mouse monoclonal antibody (Sigma F1804) was added at a concentration of 1:1,000 and further incubated for 1 hour at RT. Cells were washed 3x with 1ml of PBS and then resuspended in 250 µl of PBS containing 3% BSA and 1:2000 dilution of AF647-conjugated anti-mouse antibody (Invitrogen A-21235). After 30 min incubation at RT, cells were washed 5x with 1ml of PBS, resuspended in 3 ml of PBS and applied on top of a glass bottom microwell dish (MatTek corporation P35G-1.5-14-C) coated with poly-D-lysine (Sigma P7405). Dishes were washed with 1M KOH prior to the application of poly-D-lysine. Bacteria were left to attach to the dishes by gravity over night, and non-adherent bacteria were removed by performing 5 washes with 5 ml of PBS prior to imaging. When imaging by 4Pi-microscopy, bacterial cells were applied onto 25 mm round glass coverslips that have been previously treated with poly-D-lysine.

2D super-resolution microscopy

2D super-resolution imaging was performed with a custom-built FPALM system as previously described (5, 6). Briefly, a 405-nm laser (50 mW; CrystaLaser) and a 560-nm laser (500 mW; MPB

Communications) were used for the activation and excitation of mEos3.2, respectively. The average laser intensity of the 560-nm laser was about 2.9 kW/cm^2 while the power of 405-nm laser was increased manually during imaging to maintain an optimal density of single molecules. The fluorescent signal was collected by an oil-immersion objective lens (100 x/1.49 NA, Olympus) passed through an emission filter (ET605/70, Chroma), and focused onto a sCMOS camera (ORCA-Flash 4.0; Hamamatsu). All the images were taken at 100 frames per second (FPS) with an effective pixel size of 103 nm. Typically, 6,000 to 18,000 frames were acquired until all the molecules were exhausted. In addition, we used a custom-built focus-lock system to stabilize the focus during data acquisition, keeping the axial focal drift to less than 10 nm (7). For two-color imaging of mEos3.2 and AF647, a 642-nm laser (500 mW; MPB Communications) was used for the excitation of AF647. A custom beamsplitter (T640spxr, Chroma) and an emission filter (ET700/75, Chroma) were used to separate the fluorescent signal of AF647 from mEos3.2. Imaging was performed at 100 FPS in sequential mode, first AF647 then mEos3.2. The average 642-nm laser intensity was about 5 kW/cm^2 but no 405-nm laser was used when imaging AF647 to avoid activating mEos3.2 at the same time. For two-color registration, 100-nm fluorescent beads (TetraSpeck; Thermo Fischer Scientific) were imaged to produce a transformation matrix, which was then applied to the super-resolution images. The registration error was found to be between 4 and 8 nm. All data were analyzed using sCMOS-specific algorithms as previously described (6). Drift correction was done by using a redundancy-based cross-correlation method (8). For samples with lower molecule numbers, 100-nm fluorescent beads (Crimson, ThermoFisher) were added to the coverglass and served as markers for drift correction. To reduce over-counting, all accepted localizations in successive frames within 50 nm were considered to come from the same molecule and combined. All combined events were then binned in a 2D histogram image with a pixel size of 10 nm. For better visualization, the 2D histogram images were convolved with a 2D Gaussian kernel (σ =15 nm).

3D super-resolution microscopy

3D super-resolution imaging was performed with a custom-built W-4PiSMSN system as previously describe (9, 10). Briefly, the fluorescent signal was collected by two opposing oil objectives (100 x/1.4 NA, Olympus) coherently combined to generate an interference pattern of single molecules, which achieved isotropic super-resolution in all three dimensions. The microscope was equipped with an excitation laser at 560 nm (MPB Communications, 2RU-VFL-2000-560-B1R) and an activation laser at 405 nm (Coherent OBIS 405 LX, 50 mW). Raw data were collected with a sCMOS camera (ORCA-Flash 4.0v2, Hamamatsu) at 50 FPS. The full system design and algorithms are described in detail in reference (9).

Cluster analysis

The 2D cluster analysis procedure is shown in Supplementary Fig. S4. After carrying out the localization analysis of the super-resolution images, bacteria were manually segmented by determining the outline in the reconstructed images using ImageJ (https://imagej.nih.gov). Then localizations within each outline were assigned to each cell (Supplementary Fig. S4A). Cluster analysis was then performed for each cell in two steps. First, a DBSCAN clustering algorithm (11, 12) (search radius = 20 nm, minimum cluster size = 5) was applied to remove localizations which are sparsely distributed and not considered to be clusters (Supplementary Fig. S4B). Second, all the localization within clusters were binned into 2D histogram images and convolved with a Gaussian kernel (σ = 15 nm) (Supplementary Fig. S4C). Then a wavelet algorithm (13) and a proper threshold were used to generate a binary image (Supplementary Fig. S4D). The binary image was then applied to the Gaussian image and the center positions of each cluster were obtained by finding the local maxima of the masked image (masked image = binary image $\times$ Gaussian image) (Supplementary Fig. S4E). Finally, those localizations falling within a circle 70 nm in diameter centered at a cluster position were assigned to the cluster assuming that the clusters should be round in shape (Supplementary Fig. S4F). To estimate the cluster size, the localizations belonging to each cluster were constructed into an intensity image and fitted to a 2D Gaussian function. The cluster

size is defined as the full width at half maxima (FWHM) of the Gaussian distribution. For binning the cluster positions into 2D histogram images, we used an approach similar to one described previously (14). Briefly, all the localizations of each bacterium were plotted in x-y plane and fit to a rectangle to get the length and width of the cell (Supplementary Fig. S3B). After that, the cluster positions of each bacterium were normalized by the size of the cell and finally binned into a 2D histogram image. Considering the bacterial cell to be approximately symmetric, all clusters were placed on the first quadrant of the cell and then extended to the other three quadrants by enforcing the mirror symmetry (Fig. 1G and Fig. 2H). The cluster analysis of 4Pi images was done using the same DBSCAN algorithm (search radius = 30 nm, minimum cluster size = 5) except that the localizations are in 3D (Fig. S3). To get the 3D distribution of clusters, the localizations of each cell were fitted to a rectangle (in x-y plane) (Supplementary Fig. S3B) and circle (in y-z plane) (Supplementary Fig. S3C) to get the length and diameter of each cell. After normalization of the size of each cell, all the positions of clusters were combined (Supplementary Fig. S3E).

Estimation of the copy number of sorting platform components.

From the cluster analysis, we obtained not only the cluster number and size but also the number of localizations per cluster, which indicates the copy number of the labelled protein. However, the observed copy number differs from the real copy number due to several limiting factors. Precise single-molecule counting requires complex modeling of fluorophore blinking properties, which is beyond the scope of this study. However, to estimate the copy number of the different proteins, a simplified simulation was performed which accounts for three major factors: (i), not all mEos3.2 molecules switch to the red state, (ii), molecules can blink several times and therefore can be counted more than once and, (iii), needle complexes which by chance blink less than the cluster detection threshold are ignored and do not contribute when calculating the average copy number per cluster. The simulation assumed the following conditions: (1) The detectable molecule number in each cluster follows a Poisson distribution with a mean

of λ = real copy number × p, where p = 0.6 is the probability that a fluorescent protein is detected by our microscope. The factor 0.6 is derived from the assumption of 42% of mEos3.2 proteins to be photoactivated to the detectable form (15) multiplied with by a factor of 1.5 which is assumed to be the number of average blinking events for each molecule (16); (2) the cluster diameter was set to 25 nm which is the diameter of PrgH and we assume the other proteins are distributed in clusters of similar diameter; (3) the average localization precision is ~15 nm. Based on these assumptions, we simulated localizations of individual clusters similar to Supplementary Fig. S1B and performed cluster analysis of the simulated data using the same algorithm and parameters (search radius = 20 nm, minimum cluster size = 5) as for the real images. For each data point shown in Supplementary Fig. S6A, 10,000 clusters were generated and analyzed to get the mean and standard deviation values which were used to create a calibration curve. Based on this calibration curve, we translated observed copy number values (Supplementary Fig. S6B) into corrected copy number values (Supplementary Fig. S6C). The corrected copy number of 23 ± 5 for PrgH, which we obtained from the simulation, agrees well with the value of 24 from single particle cryo EM (Supplementary Fig. S1A) and supports the validity of our simulation approach.

References

1. Hoiseth SK & Stocker BA (1981) Aromatic-dependent *Salmonella typhimurium* are non-virulent and effective as live vaccines. *Nature* 291:238-239.
2. Kaniga K, Bossio JC, & Galan JE (1994) The Salmonella typhimurium invasion genes invF and invG encode homologues of the AraC and PulD family of proteins. *Mol Microbiol* 13(4):555-568.
3. Galán JE & Curtiss III R (1990) Expression of *Salmonella typhimurium* genes required for invasion is regulated by changes in DNA supercoiling. *Infect. Immun.* 58:1879-1885.
4. Lara-Tejero M & Galan JE (2009) The Salmonella Typhimurium SPI-1 type III secretion translocases mediate intimate attachment to non-phagocytic cells. *Infect Immun* 77:2635-2642.
5. Laplante C, Huang F, Tebbs I, Bewersdorf J, & Pollard T (2016) Molecular organization of cytokinesis nodes and contractile rings by super-resolution fluorescence microscopy of live fission yeast. *Proc. Natl. Acad. Sci. U. S. A.* 113:E5876-E5885.
6. Huang F*, et al.* (2013) Video-rate nanoscopy using sCMOS camera-specific single-molecule localization algorithms. *Nat Methods.* 10:653-658.

7. Lin Y*, et al.* (2015) Quantifying and optimizing single-molecule switching nanoscopy at high speeds. *PLoS One* 10(5):e0128135.
8. Wang Y*, et al.* (2014) Localization events-based sample drift correction for localization microscopy with redundant cross-correlation algorithm. *Opt Express* 22(13):15982-15991.
9. Huang F*, et al.* (2016) Ultra-High Resolution 3D Imaging of Whole Cells. *Cell* 166:1028-1040
10. Del Viso F*, et al.* (2016) Congenital Heart Disease Genetics Uncovers Context-Dependent Organization and Function of Nucleoporins at Cilia. *Dev Cell*.
11. Shivanandan A, Unnikrishnan J, & Radenovic A (2015) Accounting for limited detection efficiency and localization precision in cluster analysis in single molecule localization microscopy. *PLoS One* 10(3):e0118767.
12. Ester M, Kriegel H-P, Sander J, & Xu X (1996) A density-based algorithm for discovering clusters in large spatial databases with noise. *Second International Conference on Knowledge Discovery and Data Mining*, pp 226-231.
13. Olivo-Marin JC (2002) Extraction of spots in biological images using multiscale products. *Pattern Recognition* 35(9):1989-1996.
14. Wang WQ, Li GW, Chen CY, Xie XS, & Zhuang XW (2011) Chromosome Organization by a Nucleoid-Associated Protein in Live Bacteria. *Science* 333(6048):1445-1449.
15. Durisic N, Laparra-Cuervo L, Sandoval-Alvarez A, Borbely JS, & Lakadamyali M (2014) Single-molecule evaluation of fluorescent protein photoactivation efficiency using an in vivo nanotemplate. *Nature Methods* 11(2):156-+.
16. Zhang M*, et al.* (2012) Rational design of true monomeric and bright photoactivatable fluorescent proteins. *Nat Methods*. 9:727-729.

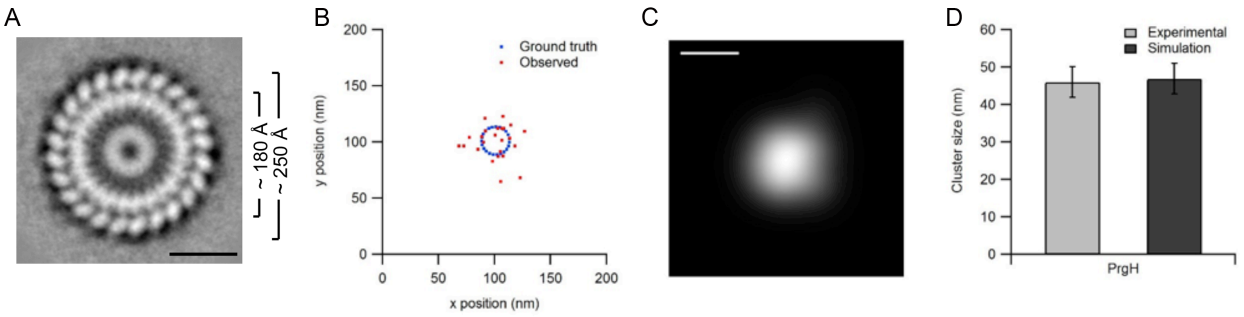

Supplementary Fig. S1. Simulation of cluster size. **a**, *En face* class-average derived from single particle analysis from negatively stained electron microscopy images of inner rings substructures. The ring substructure is organized in two larger concentric rings with different diameters (~180Å and ~250Å) and 24 molecules of PrgH form the outer ring. Bar=10nm [adapted from Schriadt et al. PLoS Pathogens 6: e1000824(2010)]. **b**, PrgH assembles into a ~ 25 nm ring made up of 24 copies of this protein (blue). However, after convolution with the localization precision (σ = 15 nm), we can no longer observe the ring (red). This means that our resolution (~35 nm, limited by the photon output of mEos3.2) is not sufficient to resolve the ring structure of the PrgH clusters. **c**, The observed localizations were convolved with a Gaussian kernel (σ = 15 nm) and fitted to a 2D Gaussian function to estimate the cluster size (FWHM). This procedure mimics the procedure in which the cluster size of the real images was determined. Scale bar: 50 nm. **d**, The cluster size (47 ± 4 nm, mean ± standard deviation) from the simulation (1,000 clusters) is consistent with what we observed from real images (46 ± 4 nm, mean ± standard deviation).

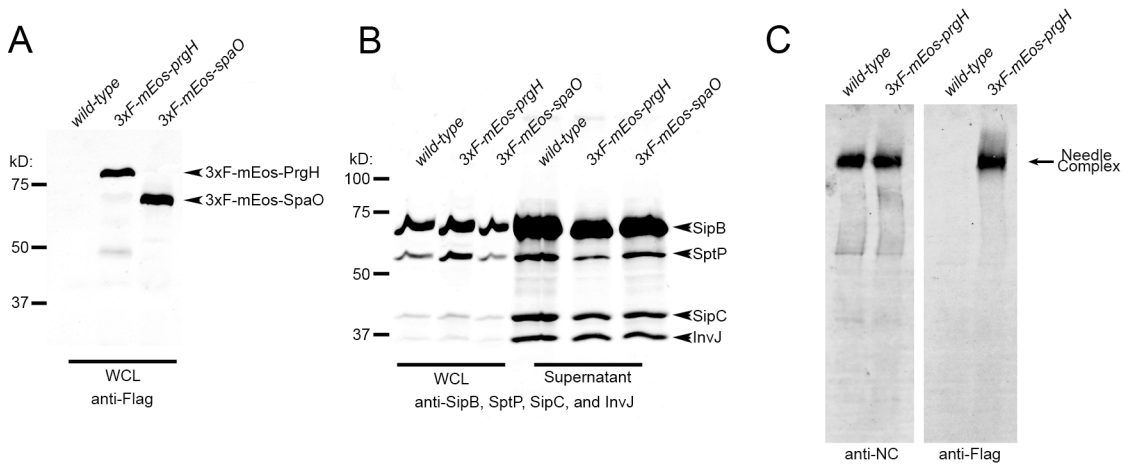

Supplementary Fig. S2. Functional characterization of the mEos-PrgH protein fusion.**. a**, Total cell lysates of wild type *S.* Typhimurium and isogenic strains expressing FLAG-tagged mEos3.2-PrgH or mEos3.2-SpaO from the native chromosomal context were analyzed by western immunoblot with an antibody directed to the FLAG epitope. The observed bands exhibited motilities consistent with the expected molecular weights of the protein fusions indicating no separation of the mEos3.2 tag from the tagged proteins. **b**, The functionality of the different chromosomally-encoded mEos3.2 fusion proteins was assayed by examining the ability of the different strains to secrete different type III secreted protein (i. e. SipB, SptP, SipC and InvJ) . Whole cell lysates (WCL) and culture supernatants of the same strains were examined by western immunoblot analysis for the presence of the type III secreted proteins SipB, SptP, SipC and InvJ with monoclonal antibodies directed to these proteins. **c**, The incorporation of mEos3.2-PrgH into full assembled needle complexes, a measure of its functionality, was assayed by examining isolated needle complexes for the presence of mEos3.2-PrgH by blue-native gel electrophoresis combined with western blot. Preparations from wild type *S.* Typhimurium or an isogenic mutant expressing mEos3.2- and FLAG tagged PrgH were analyzed by blue native gel electrophoresis using antibodies to the needle complex (NC) or the the FLAG tag.

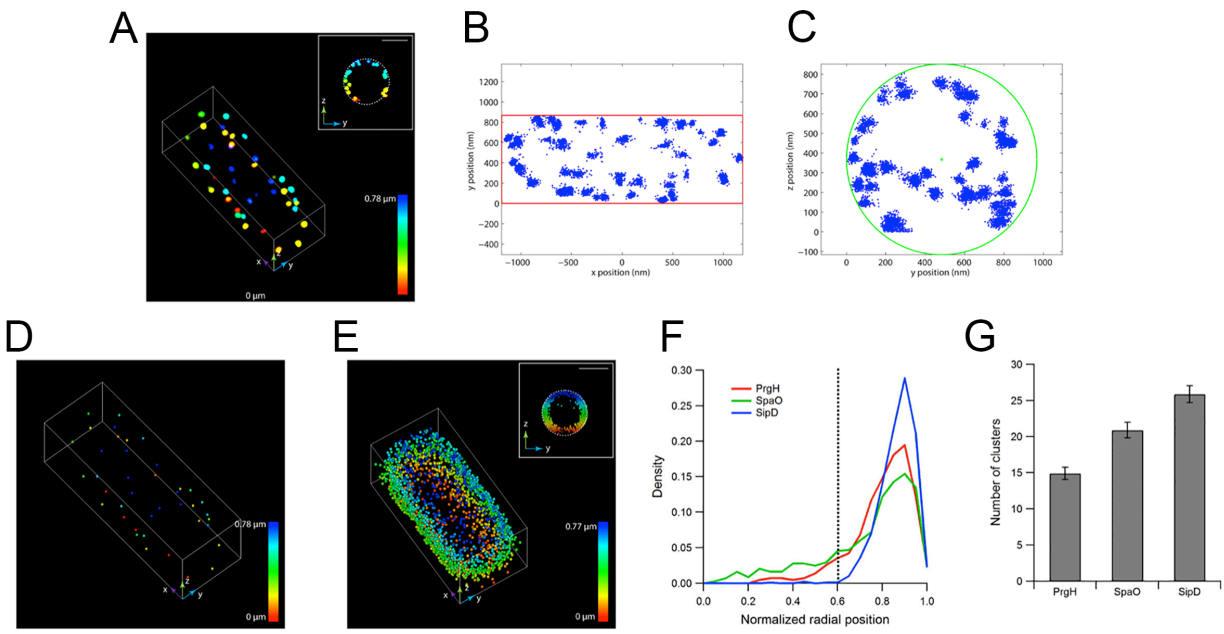

Supplementary Fig. S3. Cluster analysis of 3D super-resolution imaging. **a**, An example 4Pi image (3D) of a bacterial cell labeled with an AF647-labelled antibody directed to a FLAG epitope in SipD. The z-position information of the localizations is color-coded according to the color scale bar. Inset image shows the y-z view of the localizations. Inset scale bar: 500 nm. **b**, All the localizations from (**a**) were plotted in x-y plane and fitted to a rectangle (red) to obtain the length of the cell. **c**, All the localizations from (**a**) were plotted in y-z plane and fitted to a circle (green) to obtain the diameter of the cell. **d**, 3D cluster analysis result of (**a**) using a DBSCAN algorithm. Each dot represents the center of a cluster. **e**, The center positions of the clusters from 78 cells (labeled with an AF647-labelled antibody directed to a FLAG epitope in SipD) were normalized according to the length and diameter of each cell and plotted together. Each dot represents the center position of a cluster. Inset image shows the y-z cross section of the center half of the cell. Inset scale bar: 500 nm. **f**, Normalized cluster densities along the radial direction of bacteria cells labeled with mEos3.2-PrgH, mEos3.2-SpaO and AF647-labelled antibody directed to a FLAG epitope in SipD, respectively. Only clusters within the center half of the cell were used for the density calculation. The black dashed line indicates the position where 99% of the SipD-associated clusters are considered to be at the bacterial periphery. The position was used as the threshold to differentiate the periphery of the bacteria and the cytoplasm for the PrgH- and SpaO-associated clusters. We found ~93% of the PrgH clusters and ~80% of the SpaO clusters were located at the bacterial periphery. **g**, Number of fluorescent clusters associated with the indicated proteins per bacteria overserved in 4Pi imaging. Numbers represent the mean ± standard error (PrgH: 14.90 ± 0.86, 58 cells; SpaO: 20.89 ± 1.11, 65 cells; SipD: 25.86 ± 1.16, 78 cells).

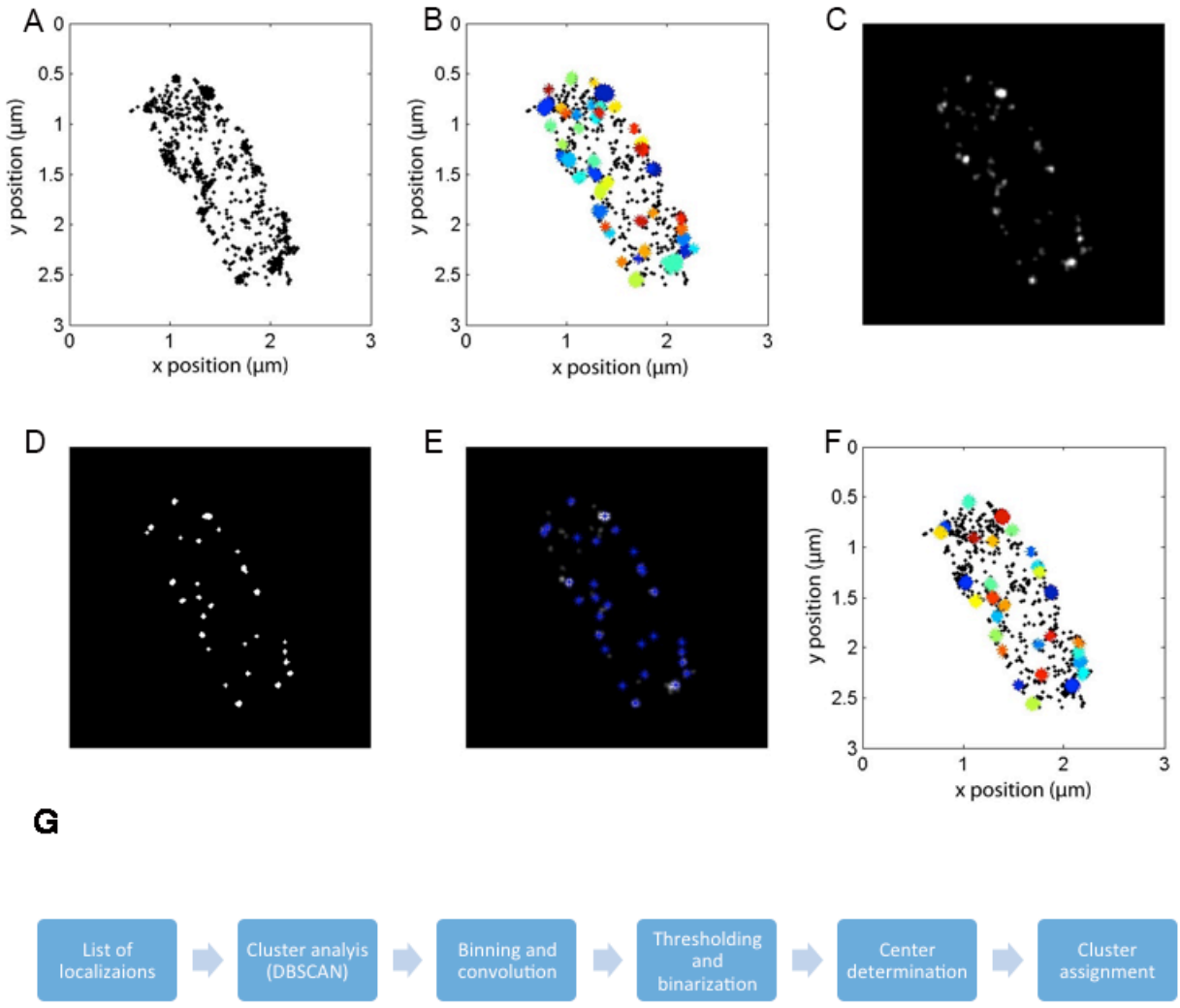

Supplementary Fig. S4. Cluster analysis of super-resolution images. **a**, Example of localizations in a bacterial cell. Each black dot represents a localization event. **b,** Cluster analysis using the DBSCAN algorithm. Each cluster was displayed with a different color and black dots represent localizations not associated with clusters. **c**, The localizations within clusters are binned into a 2D histogram image and convolved with a Gaussian kernel (s = 15 nm). **d**, A wavelet algorithm and a proper threshold were used to generate a binary image (**c**), to remove the localization outside of the mask. **e**, The positions of each cluster were obtained by finding the local maxima of the masked image [masked image = image in (**c**) x image in (**d**)]. **f**, Those localizations within 35 nm of a cluster position [blue stars in (**e**)] were assigned to the cluster and displayed with one color. See Materials and Methods for further details. **g,** Diagram of the cluster analysis strategy.

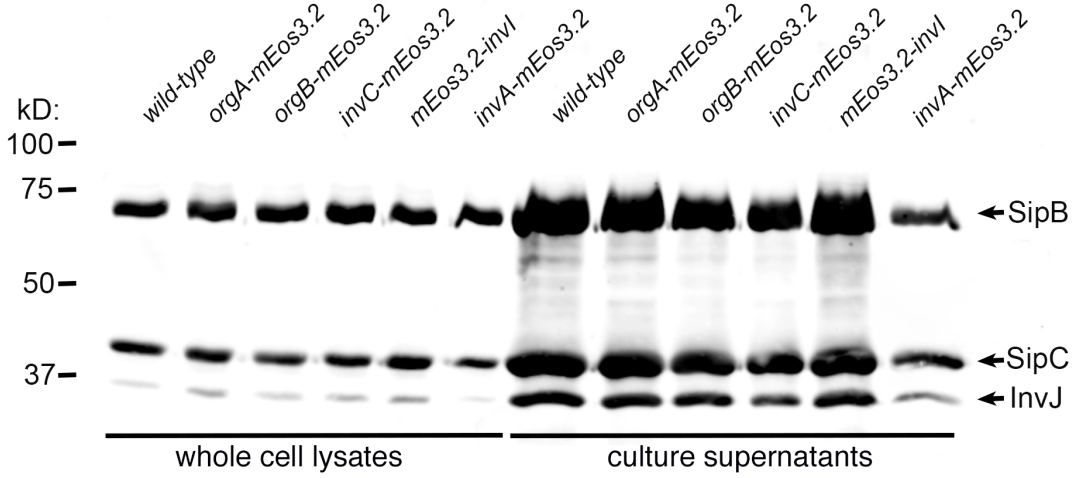

Supplementary Fig. S5. Functional characterization of the mEos-protein fusion to sorting platform and export apparatus components. The functionality of the different chromosomally-encoded mEos3.2 fusion proteins was assayed by examining the ability of the different strains to secrete different type III secreted protein (i. e. SipB, SipC and InvJ) . Whole cell lysates and culture supernatants of wild type *S.* Typhimurium and isogenic strains expressing the indicated mEos3.2-fusion proteins from the native chromosomal context were analyzed by western immunoblot for the presence of the type III secreted proteins SipB, SptP, SipC and InvJ with monoclonal antibodies directed to these proteins.

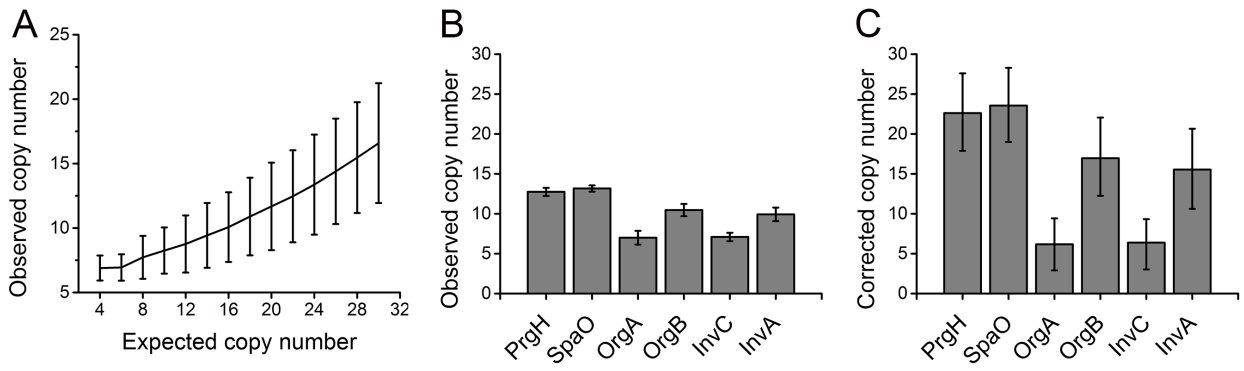

Supplementary Fig. S6. Estimation of the copy number of the type III secretion system components. **a**, Simulation of the relationship between the observed and expected copy number for the type III secretion system components. Observed numbers in the simulation are the mean ± standard deviation of 10,000 clusters. **b** and **c**, Observed (**b**) and corrected (**c**) copy number of the indicated components of the type III secretion system. Numbers are are the mean ± standard deviation (see Materials and Methods for experimental details).

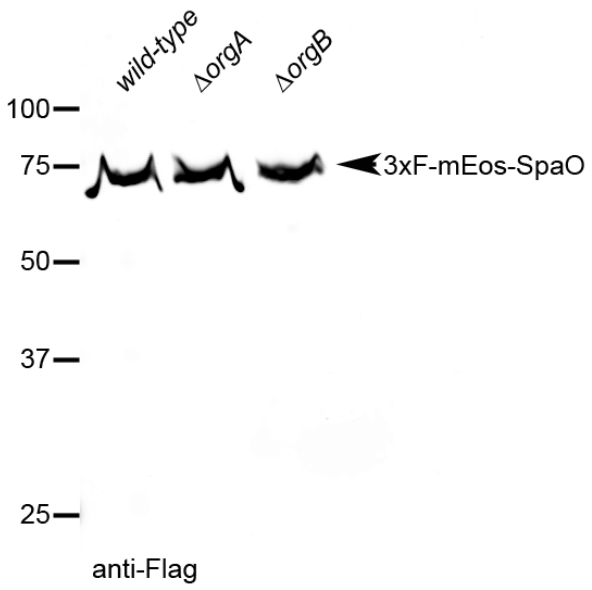

Supplementary Fig. S7. Stability of mEos3.2-SpaO in the absence of sorting platform components. Total cell lysates of wild type *S.* Typhimurium and isogenic strains expressing FLAG-tagged mEos3.2-SpaO from the native chromosomal context were analyzed by western immunoblot with an antibody directed to the FLAG epitope.

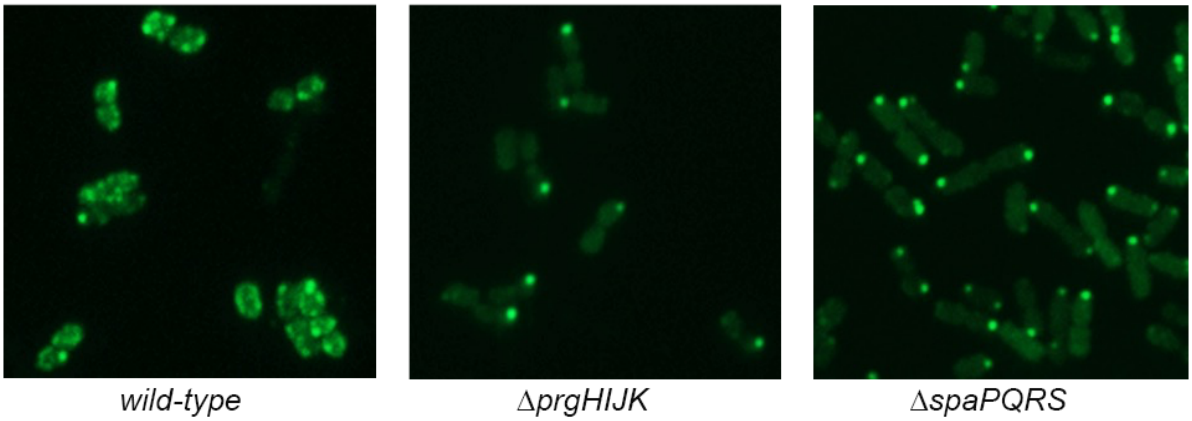

Supplementary Fig. S8. Confocal microscopy images of *S.* Typhimurium strains (wild type and the isogenic Δ*prgH*/Δ*prgI*/Δ*prgJ*/Δ*prgK* and Δ*spaP*/Δ*spaQ*/Δ*spaR*/Δ*SpaS* isogenic mutants, as indicated) expressing a functional superfolder GFP-SpaO protein fusion expressed from its native chromosomal context.

Supplementary Table S1. Cluster analysis of 2D super-resolution images

Figure	Protein (background strain)	Number of independent experiments	Number of cells analyzed	Total number of clusters	Cluster number per bacteria[1]	Cluster size FWHM[2] (nm)[1]	Copy number[1]
1	PrgH (w. t.)	4	585	7,295	12.47 ± 0.72	45.98 ± 0.05	12.94 ± 0.10
2	SpaO (w. t.)	3	595	12,710	21.36 ± 0.31	47.58 ± 0.04	13.21 ± 0.08
3	OrgA (w. t.)	3	471	4,585	9.73 ± 0.22	43.19 ± 0.06	7.24 ± 0.08
3	OrgB (w. t.)	3	642	8,661	13.49 ± 0.37	45.83 ± 0.04	10.85 ± 0.07
3	InvC (w. t.)	3	581	5,246	9.03 ± 0.23	42.90 ± 0.05	7.45 ± 0.09
3	InvI (w. t.)	2	237	-	-	-	-
3	InvA (w. t.)	3	431	5,215	12.10 ± 0.47	44.14 ± 0.06	9.17 ± 0.11
4	SpaO (Δ*orgA*)	2	545	n. a.	n. a.	n. a.	n. a.
4	SpaO (Δ*orgB*)	2	317	n. a.	n. a.	n. a.	n. a.
4	SpaO (Δ*invC*)	3	664	2,085	3.14 ± 0.15	n. c.	n. c.
4	SpaO (Δ*invI*)	4	705	8,334	11.82 ± 0.23	n. c.	n. c.
4	SpaO (Δ*prgHIJK*)	1	98	n. a.	n. a.	n. a.	n. a.
4	SpaO (Δ*spaPQRS*)	2	228	n. a.	n. a.	n. a.	n. a.
5	SopB (w. t.)	2	690	2,899	10.03 ± 0.28	45.65 ± 0.07	n. c.
5	SopB (Δ*prgHIJK*)	3	593	1,475	6.77 ± 0.28	45.03 ± 0.10	n. c.
5	SopB (Δ*spaO*)	3	543	1,174	6.28 ± 0.21	47.10 ± 0.19	n. c.

[1] : Numbers are mean ± standard error

[2]: full width at half maxima

n. a. : not applicable

n. c. : not calculated

Supplementary Table S2. Strains and plasmids used in these studies

Strain	Relevant genotype	Reference
SB2688	*mEos3.2-spaO*	This study
SB2689	*invA-mEos3.2*	This study
SB2698	*mEos3.2-spaO* Δ*prgHIJK*	This study
SB2699	*mEos3.2-spaO* Δ*orgB*	This study
SB2700	*mEos3.2-spaO* Δ*invC*	This study
SB2758	*mEos3.2-prgH*	This study
SB2777	*mEos3.2-spaO sipD-3xF*	This study
SB2778	*mEos3.2-prgH sipD-3xF*	This study
SB2792	*3xF-mEos3.2-prgH*	This study
SB2793	*3xF-mEos3.2-spaO*	This study
SB2836	*orgB-mEos3.2*	This study
SB2837	*invC-mEos3.2*	This study
SB2845	*mEos3.2-spaO* Δ*spaPQRS*	This study
SB2846	*mEos3.2-spaO* Δ*orgA*	This study
SB2847	*mEos3.2-spaO* Δ*invI*	This study
SB3052	*orgA-mEos3.2*	This study
SB3053	*3xF-mEos3.2-invI*	This study
SB3061	*3xF-mEos3.2-spaO* Δ*orgA*	This study
SB3062	*3xF-mEos3.2-spaO* Δ*orgB*	This study
SB3080	*sopB-mEos3.2-3xF*	This study
SB3100	*sopB-mEos3.2-3xF* Δ*spaO*	This study
SB3101	*sopB-mEos3.2-3xF* Δ*prgHIJK*	This study
Plasmid		
pSB3292	*pBAD-hilA*	This study